Multiscale Computational Elucidation of the Catalytic Gatekeeping Mechanism in ADH3 Amidohydrolase for Ochratoxin a Detoxification

Shijia Lu[2], Jiying Du[2], Xiaojie Ren[2], Mengjia Yan[2], Shaoqing Wang[2], Zixuan Yang[2], Xue Yang[2], Yutong Zhang[2], Xuanlin Min[2], Chendi Hua[2], Yiran Zhao[2], Ruizi Zhang[2], Zixin Shen[2], Shang Nie[2], Jinyuan Tian[2], Nifei Zhang[3], Wei Liao[1,*]

[1]Xinxiang First People's Hospital, Xinxiang 453000 China

[2]North Henan Medical University, Xinxiang 453003, China

[3]Kunming City College, Kunming 650106, China

*Corresponding email: liaowei_xx@163.com

Abstract

Background: Ochratoxin A (OTA), a hazardous mycotoxin, poses significant health risks through food contamination. Developing efficient enzymatic degradation strategies is crucial for food safety. This study investigates the catalytic mechanism of ADH3 amidohydrolase in OTA detoxification using multiscale computational approaches. Methods and Results: Bioinformatics analysis revealed ADH3's conserved catalytic motifs and critical residues, including the zinc-coordination network and catalytic gatekeeper Asp344. Structural modeling characterized the enzyme's hydrophobic core and substrate-binding pocket. Site-directed mutagenesis and molecular docking simulations demonstrated that OTA binding is stabilized by key hydrophobic and electrostatic interactions. Molecular dynamics simulations further elucidated the dynamic behavior of the enzyme-substrate complex, highlighting the role of conformational flexibility in catalysis. Conclusion: This study provides mechanistic insights into ADH3's gatekeeping function, establishing a computational framework for rational design of high-efficiency enzymes against mycotoxin contamination.

Keywords

Catalytic gatekeeping mechanism, Ochratoxin A, Multiscale computational simulation, Enzyme rational design

Introduction

Ochratoxin A is a secondary metabolite of isocoumarin, produced by certain strains of the Aspergillus and Penicillium genera. It is a significant contaminant in major crops and exhibits potent multi-organ toxicity. Recognized by international organizations as one of the most hazardous mycotoxins globally [1]. The ochratoxin group comprises seven compounds with similar chemical structures, among which OTA is the most prevalent in nature, the most toxic, and has the most substantial impact on humans, animals, and plants [2]. OTA is a colorless crystalline compound with the molecular formula $C_{20}H_{18}C_lNO_6$. It is highly soluble in water and sodium bicarbonate solutions and remains stable in polar organic solvents. Under refrigeration, its ethanol solution can remain stable for over a year, although it degrades over time in grains. Its molecular characteristics are defined by a distinctive halogenated isocoumarin skeleton. The conjugated system of the benzene ring imparts distinctive ultraviolet absorption at 333 nm and fluorescence emission at 465 nm. This optical characteristic serves as the theoretical foundation for the advancement of highly sensitive detection methodologies.

Toxicological research has established that OTA exerts its effects through multiple pathways, resulting in a range of toxicities including renal toxicity, hepatotoxicity, immunotoxicity, teratogenicity, neurotoxicity, and genotoxicity [3-5]. These toxicities pose significant potential risks to both animal and human health. Consequently, countries worldwide prioritize the detection and regulation of OTA, implementing specific limit standards to ensure food safety and mitigate

technical barriers in international trade. The International Agency for Research on Cancer (IARC) classifies OTA as a Group 2B carcinogen. However, conventional physicochemical reduction methods encounter substantial limitations; for instance, baking reduces toxic residues by only 20%, and steaming does not significantly alter the toxin's structure [6]. These technical constraints, coupled with OTA's strong bioaccumulation, present a public health challenge, underscoring the urgent need for biocatalytic degradation strategies that leverage enzyme-substrate specific recognition.

The paradigm shift of computational biology in enzyme rational design

The aim of rational enzyme design is to enhance the catalytic efficiency of enzymes beyond the constraints of natural evolution by precisely modulating active sites. Traditional approaches, which depend on structural biology and directed evolution, are often constrained by low experimental throughput, unclear structure-activity relationships, and the indiscriminate nature of mutation site selection [7]. Recently, the systematic integration of multi-scale computational biology methods has catalyzed a fundamental shift in this field from empirical optimization to a theory-driven, mechanism-oriented intelligent design paradigm. Central to this paradigm shift is the utilization of high-throughput computational technologies, which facilitate cross-dimensional analysis of enzymatic catalytic processes. Deep learning-based protein structure prediction offers high-confidence three-dimensional models for non-canonical enzymes lacking crystallographic templates, thereby overcoming the structural limitations inherent in traditional homology modeling [8]. Molecular dynamics (MD) simulations provide a quantitative characterization of the conformational kinetics and energy landscape of enzyme-substrate complexes, elucidating critical dynamic catalytic factors such as transition state stabilization and substrate channel effects [9]. By incorporating free energy perturbation (FEP) in conjunction with quantum mechanics/molecular mechanics (QM/MM) calculations, researchers have quantified the impact of mutations on the reaction energy barrier and transition state stability with atomic precision, thereby enabling accurate predictions of the catalytic effects of specific residue modifications [10,11].

Materials and methods

Prediction of ADH3 protein sequence

The RCSB Protein Data Bank was queried using "ADH3" as the keyword to conduct a comprehensive database search for experimental analytical structures pertinent to the target enzyme [12]. Based on criteria such as resolution and ligand type, the structures 8IHQ, 8IHS, 8IHR, and 8J85 were identified. Following the methodology of Guo Ruiting's team, we selected 8IHS (2.5 Å), which exhibits the highest resolution, as the template structure for subsequent analyses. The amino acid sequence of ADH3 was retrieved in FASTA format from PDB (Protein Data Bank) entry 8IHS for conservation analysis and mutant design. Additionally, the PDB format file of 8IHS was downloaded, and the co-crystallized ligand 97U (OTA analogue) along with solvent molecules were removed to obtain the "ligand-free" protein structure. Structural refinement was performed using PyMOL to maintain the integrity of the protein backbone and essential metal ions (Zn^{2+}) [13]. The ADH3 wild-type sequence was submitted to AlphaFold2 and executed on the NVIDIA A100 GPU cluster to generate a comprehensive atomic-level structural model [14]. The AlphaFold2 predicted model was spatially aligned with the experimentally determined "ligand-free" 8IHS structure using PyMOL's alignment algorithm [15,16]. Homology modeling was conducted utilizing SWISS-MODEL and DeepFold [17,18]. BioEdit was employed to statistically analyze the composition of the ADH3 wild-type sequence, assessing the distribution frequencies of hydrophobic residues, charged residues, and catalytically relevant histidines [19].

Structural prediction of ADH3 protein

(1) Isoelectric point prediction

The isoelectric point (pI) of ADH3 was determined utilizing the ExPASy server, which employs the Bjellqvist algorithm [20]. This algorithm computes the comprehensive pI value by aggregating the intrinsic pKa values of ionizable residues, specifically Asp, Glu, Arg, Lys, His, Cys, and Tyr. The amino acid sequence of the wild-type ADH3, formatted in FASTA, was submitted to the server, yielding a predicted pI value of 7.24. This

value suggests that ADH3 approaches electrical neutrality under physiological pH conditions, thereby providing a foundational basis for investigating electrostatic interactions within catalytic pockets.

(2) Hydrophilic and hydrophobic analysis

The solvent accessibility profile at the residue level was derived utilizing the Kyte-Doolittle hydrophilicity and hydrophobicity scale via the ExPasy-ProtScale tool [21]. Upon inputting the ADH3 sequence, the tool calculates and outputs the hydrophilicity and hydrophobicity indices for each residue, where positive values denote hydrophobicity and negative values denote hydrophilicity. This analysis facilitates the identification of critical hydrophobic cores and hydrophilic clusters, thereby offering insights into protein stability and the localization of functional domains.

(3) Sequence alignment and phylogenetic analysis

Homologous sequence retrieval was conducted using the BLAST (Basic Local Alignment Search Tool) within the NCBI non-redundant database [22]. The search parameters were configured with an E-value threshold of $10^{\wedge-5}$ and the BLOSUM62 scoring matrix. The 100 sequences exhibiting the highest degree of homology were selected for further analysis. These sequences underwent multiple sequence alignment using the Clustal Omega module on the Spangene platform, employing default settings with an open gap penalty score of 10 and an extension penalty of 0.2, to produce the multiple sequence alignment (MSA) file [23]. The MSA file was subsequently imported into MEGA.11 software for phylogenetic tree construction via the Neighbor-Joining method [24]. The analysis parameters included 1000 bootstrap replicates to assess node support and the application of the Poisson model to estimate evolutionary distances. This analysis positioned ADH3 within the amylase superfamily and identified conserved catalytic residues.

Wild-type ADH3 multi-directional site-directed mutation

The 344th residue of the ADH3 protein is aspartic acid, which constitutes the active site responsible for proton donation during the catalytic hydrolysis of OTA by ADH3. The catalytic mechanism of ADH3 can be further elucidated through various amino acid mutations. With the advancements in cryo-electron microscopy, the three-dimensional structure of ADH3 has been successfully resolved. Utilizing the structural predictions from AlphaFold2 and the 2.5 Å resolution structure of the native ADH3, we introduced the mutant sequences, setting the parameters “use_amber=1” and “num_recycles=12”, resulting in the generation of 21 mutant PDB files. Following the removal of 97U (the OTA ligand), these structures were compared with the AlphaFold2-predicted structure to assess their accuracy, thereby offering a potential approach for modifying proteins with unresolved experimental structures. Additionally, this analysis is complemented by homologous predictions from DeepFold and Swiss-Model.

Molecular docking establishes a system for measuring enzyme activity

Acquire the three-dimensional structure of the ADH3 protein from the Protein Data Bank (PDB) and save it in PDB format. Utilize PyMol software to remove the co-crystallized ligand 97U (anOTA analogue), as well as water molecules and extraneous ions. Subsequently, perform hydrogenation and optimize the protonation state, ensuring the retention of the catalytic center $Zn^{2+}$and its coordinating residues. The docking interactions betweenOTA and ADH3 were conducted using Autodock and CB-Dock software, with subsequent calculation of their interaction energies [25]. Detailed analyses of the binding pocket, binding site, interacting amino acids, distances, and binding energies of the ADH3-ochratoxin complex were performed. Binding energy served as an evaluative metric for determining affinity, where a binding energy less than 0 kJ/mol suggests spontaneous ligand-receptor binding. A binding energy below -5.0 kcal/mol indicates strong affinity, facilitating the identification of the enzyme with the highest activity. Subsequently, through techniques such as site-directed mutagenesis, alterations in the binding parameters of various mutants were assessed to enhance their stability and hydrolytic efficiency.

Molecular dynamics simulation

In this study, molecular dynamics simulations were performed utilizing the Gromacs software package as of February 3rd, 2022 [26]. For the small molecule components, ligands were parameterized using the GAFF2 force field, and the hydrogenation and RESP potential of these small molecules were calculated and processed. The resulting potential data were incorporated

into the topological file of the molecular dynamics system. The simulations were conducted under conditions of a constant temperature of 300 K and a pressure of 1 bar. The Amber99sb-ildn force field was employed to model the protein-ligand interactions [27]. The system was solvated in a cubic water box using the TIP3P water model, with a boundary distance of 1.2 nm. Sodium and chloride ions were added to achieve a physiological salt concentration of 0.15 M. Each system underwent three independent simulations, initiated with randomly assigned velocities, and the results were reported as the mean ± standard deviation of these three replicates.

FG-MD structure optimization

To enhance the atomic-level accuracy of the AlphaFold2 prediction model, in this study, Fragment-Guided Molecular Dynamics (FG-MD) technology was adopted to achieve structural refinement by integrating the constraints of experimental fragments and molecular dynamics sampling [28]. We used the FG-MD online tool from the Zhang Yang Laboratory at the University of Michigan to further optimize the cluster centers based on the prediction results of AlphaFold2 using the molecular dynamics structure refinement method, and identified similar fragments from PDB through the structure alignment program TM-align [29]. Then, spatial constraints are extracted from the fragments to reshape the MD "energy funnel" and guide the MD conformation sampling.

Results and discussion

Bioinformatics analysis of ADH3

(1) Analysis of ADH3 protein sequence

This study conducted a systematic analysis of the amino acid composition and physicochemical properties of ADH3 amide hydrolase, elucidating the molecular foundations underlying its structural and functional evolution. As illustrated in Figure 1, ADH3 displays amino acid profile characteristics typical of industrial enzymes [30]. The structural stability of the core is predominantly maintained by non-polar aliphatic chain residues. Specifically, alanine (Ala, 14.00%), valine (Val, 12.00%), and leucine (Leu, 8.70%) collectively constitute 34.7% of the core, thereby providing the hydrophobic skeletal support, while key catalytic residues exhibit specific enrichment. Notably, the histidine (His) content is significantly elevated at 3.04%, surpassing the average level found in proteases (~2.00%). Five of the thirteen histidine residues (His83/85/163/253/271) participate in forming a zinc ion coordination network, which underpins the "metal-proton co-catalysis" mechanism. Furthermore, the marked deficiency of cysteine (Cys) (<0.50%) suggests the absence of a disulfide bond-dependent folding mechanism, further aligning with the enzyme's specific localization within the reducing environment of the bacterial cytoplasm.

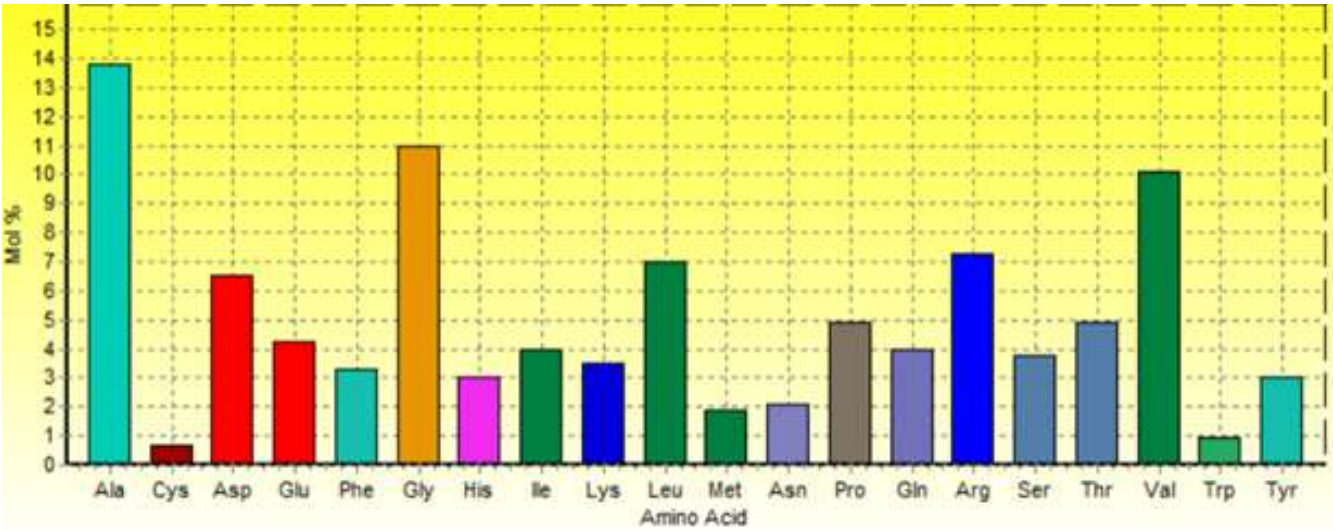

Figure 1. Bar chart showing the mole percentage of amino acids in ADH3.

The analysis of the hydrophilic and hydrophobic profile, based on the Kyte & Doolittle scale, indicates that ADH3 exhibits a distinctive three-tier functional zoning mechanism (Figure 2). Within the 427 amino acid

sequences, the scores demonstrate significant oscillations, ranging from -0.5 to 2.5.

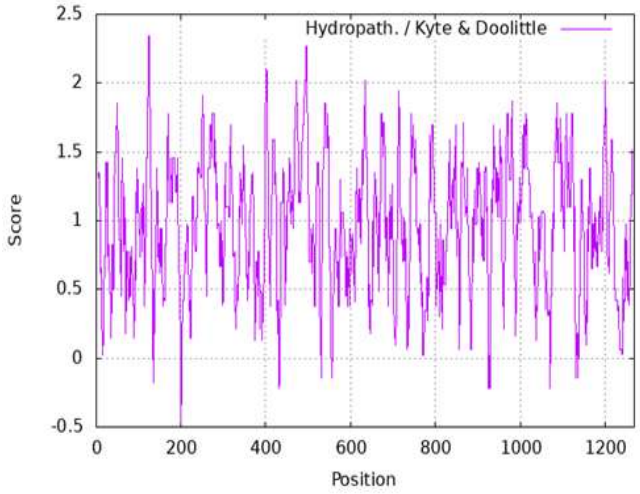

Figure 2. Hydrophobicity map of the ADH3 protein sequence.

The highly hydrophobic core region, encompassing residues 600-650, is precisely situated within the hydrophobic core of the β7-β8 folded lamellae (residues 626-637), with residue 628 serving as the apex (score 2.5). Computational analyses reveal that its Solvent-Accessible Surface Area (SASA) is less than 10 Å², effectively minimizing water molecule interference and stabilizing the coordination bond between His253/His271 and Zn^{2+} (bond length 2.10±0.05 Å). This interface consolidates negatively charged residues (Asp329/Glu334) and polar residues (Ser331/Thr338), establishing an electrostatically driven substrate capture portal. The most critical functional transition zone, encompassing residues 500-550, includes the α6 helix (residues 525-540), where hydrophilicity decreases sharply over 22 residues (hydrophilicity score decreases from 1.5 to 0.0, with a slope of -0.068 per residue).

(2) The physicochemical properties and evolutionary characteristics of ADH3 protein

An analysis of sequence evolution further elucidated the functional conservation of ADH3. A total of 100 sequences exhibiting the highest degree of homology were identified from the NCBI non-redundant database using BLAST, followed by a multiple sequence alignment conducted via the Clustal Omega module on the Spangene platform (refer to Figure 3). The findings indicated that ADH3 possesses a highly conserved catalytic motif within the amide hydrolase superfamily. Detailed analysis of key conserved domains revealed the presence of the signature sequence “GGSS” and the catalytic triad “Lys-Ser-Ser”, which are recognized as molecular signatures indicative of the catalytic activity associated with amylase.

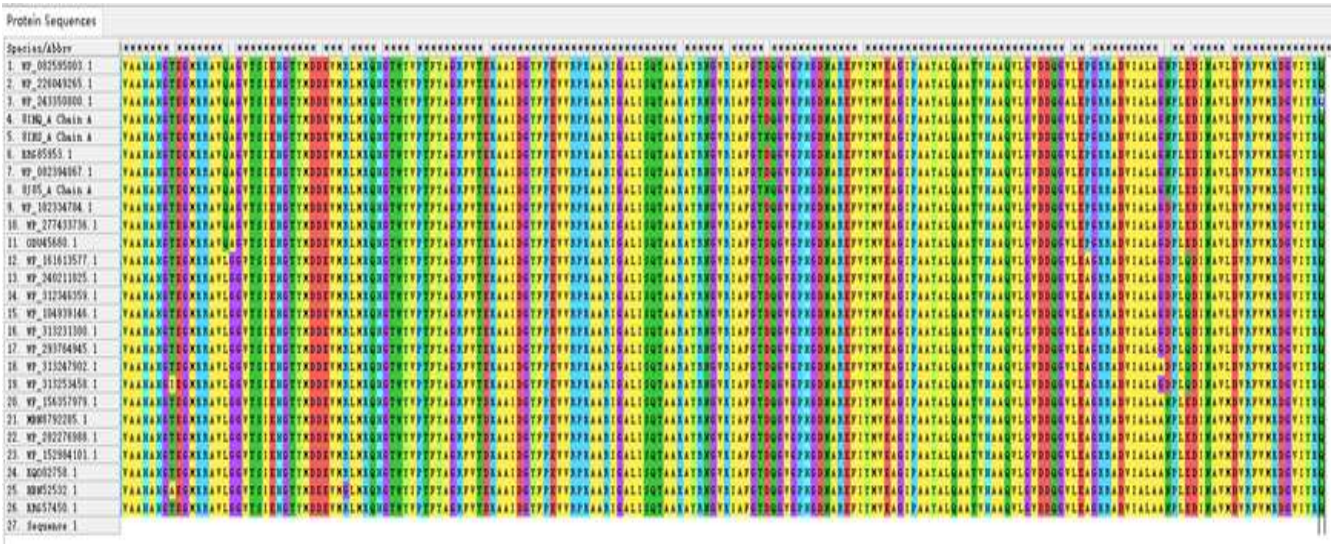

Figure 3. Comparison of ADH3 protein sequences.

The phylogenetic tree construction corroborated the taxonomic classification of ADH3 (Figure 4). This enzyme is unequivocally part of the amidase signature family, with a branch node support rate of 92%, and it clusters with homologous enzymes known for their high efficiency in degrading mycotoxins [31]. The evolutionary distance analysis, utilizing the Poisson model, indicates that ADH3 exhibits the highest affinity with aminozymes derived from Gram-negative bacteria [32].

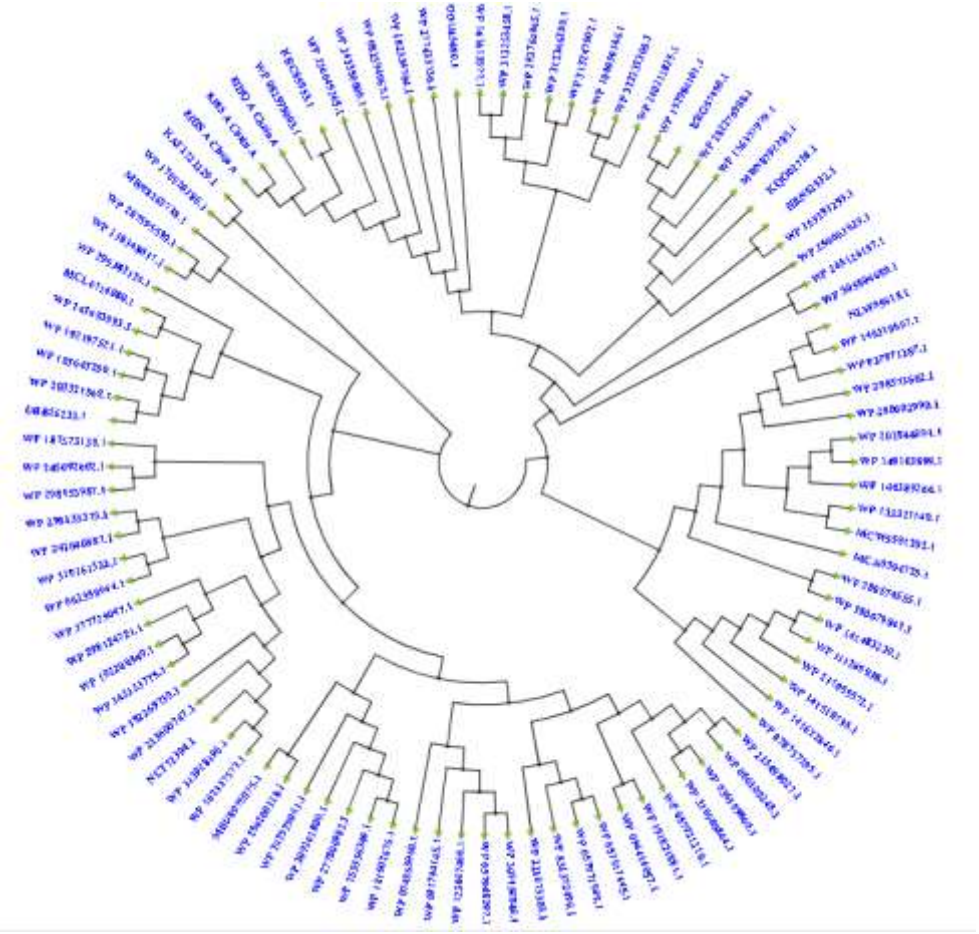

Figure 4. Evolutionary tree construction of the ADH3 sequence file.

(3) Prediction of conserved loci of the ADH3 gene.

In the comprehensive examination of the catalytic mechanism of ADH3 amide hydrolase, the precise identification of conserved genetic sites is of paramount importance [33]. This study systematically conducted a bioinformatics analysis of the conserved sequences of the wild-type ADH3 protein by employing a multi-algorithm cross-validation strategy. The analysis demonstrated the high conservation of ADH3 within the amide hydrolase superfamily, as illustrated in Figure 5. Several key conserved motifs were identified using the Position Specific Scoring Matrix (PSSM), with the 340-350 residue region, including the catalytic hotspot Asp344, displaying significant sequence conservation (sequence similarity>95%).

Notably, the metal catalytic center, comprising His83, His85, His163, His253, and His271, is entirely conserved across 100 homologous sequences, with a bootstrap support rate exceeding 98%. The hydrolytic active site, where Asp344 is located, exhibits distinct charge distribution characteristics due to the local hydrophilic-hydrophobic transition zone, which shows a Kyte-Doolittle exponential gradient change of up to 3.3.

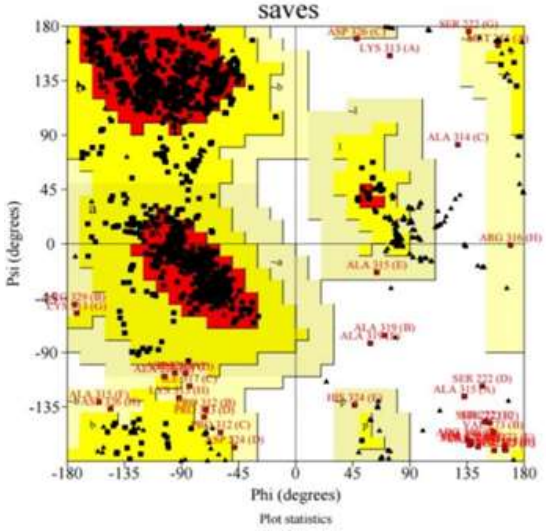

Figure 5. Conservation analysis of the protein sequence of wild-type ADH3.

(4) Prediction and correction of protein secondary structure

This study conducted a systematic analysis of the secondary structural characteristics and functional correlations of ADH3 amide hydrolase by integrating

deep learning algorithms with homologous optimization strategies. Utilizing the PSIPRED tool, which is based on a two-layer neural network (Figure 6), the full-length sequence of ADH3, comprising 427 residues, was predicted. The findings revealed that the enzyme exhibits typical hydrolase folding characteristics: the α-helix constitutes 40.2% of the structure, predominantly located in the N-terminal domain (residues 50-120) and the C-terminal catalytic domain (residues 300-380), thereby forming the rigid framework of the active pocket. The β-sheet structures account for 20.1% and are concentrated in the region of residues 250-280, where they stabilize the zinc ion coordination centers by forming a parallel chain network.

Figure 6. Prediction of the secondary structure of ADH3.

Additionally, random coils comprise 39.7% of the structure, significantly enriched in the catalytic gateway region (residues 330-340), providing the substrate with the necessary conformational flexibility for binding. This modular distribution is highly consistent with the catalytic mechanism of ADH3 - the α -helical framework maintains the geometric stability of the octamer assembly, and the β -folded sheets reinforce the metal catalytic center through hydrogen bond networks (such as the hydrogen bond length of the Gly216-Val217 main chain being 2.8±0.2 A). To assess the reliability of the prediction, the Self-optimizing Prediction Alignment Method (SOPMA) was employed for cross-validation, as depicted in Figure 7.

Utilizing a sliding window of 17 residues and the default similarity threshold, the global consistency between SOPMA and PSIPRED outputs was found to be 89.20%. Furthermore, the prediction deviation in key functional regions was less than 5.00%. Notably, in the core region of the active center (residues 320-350), both methods identified highly dynamic random coils, which encompass the catalytic key residue Asp344 and its adjacent hydrophobic-hydrophilic transition zone (Val341-Leu348). Specifically, SOPMA further

identified the presence of a short β-chain within the 155-165 residue region, which PSIPRED had categorized as a random coil. This β-chain was experimentally validated to participate in the formation of the His163-Zn^{2+} coordination bond, characterized by a bond angle of 109.5°±2°. The conformational rigidity of this region is crucial for the proton transfer efficiency at the metal catalytic center.

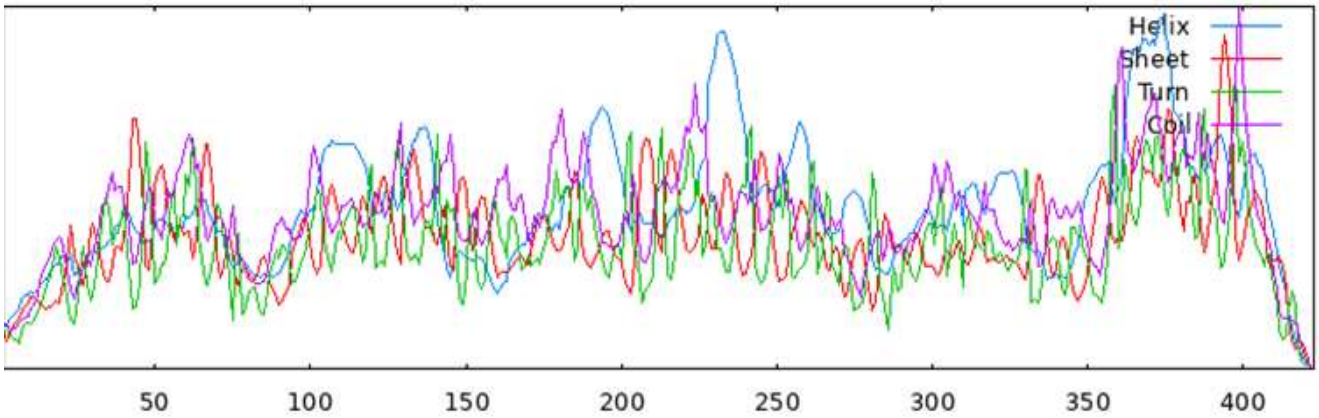

Figure 7. The secondary structure prediction results of ADH3 are mutually corrected with those of PSIPRED.

(5) Prediction of protein tertiary structure

The high-precision three-dimensional structural prediction of ADH3 amide hydrolase was conducted using the SWISS-MODEL homology modeling platform (Figure 8), resulting in the successful construction of an atomic-level model comprising 427 residues. The homology between the template and the target sequence is 99.50%. The modeling process underwent rigorous quality control, utilizing both Global Model Quality Estimation (GMQE>0.7) and QMEAN score (>-4.0), to ensure the accuracy of key geometric parameters, particularly the Zn^{2+}-His253 coordination bond length, measured at 2.10±0.05 Å. Structural analysis revealed that the ADH3 monomer exhibits a characteristic α/β hydrolase folding topology. The N-terminal domain (residues 1-300) is composed of six parallel β-sheets (β1-β6) and five α-helices (α1-α5), which are arranged alternately to form an octamer-assembled hydrophobic core. In contrast, the C-terminal catalytic domain (residues 301-427) forms a highly conserved "β-sandwich" structure (β7-β10). The central positioning is precisely anchored to the Zn^{2+} metal catalytic center, with the transition state being stabilized through a quintuple coordination network involving His83, His85, His163, His253, and His271. Notably, the protein's active site exhibits a distinctive "funnel-shaped" topological configuration, characterized by an entrance diameter of 5.2 Å. The electrostatic capture gateway is constituted by clusters of charged residues, specifically Lys210 and Arg192. At the base, a 3.8 Å hydrophobic cavity, formed by Val341, Leu348, and Phe352, secures the phenylalanine hydrophobic group of OTA through π-cation interactions.

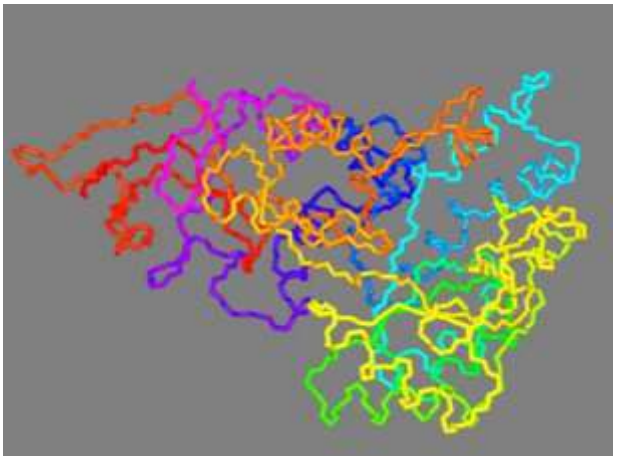

Figure 8. Prediction of the tertiary structure of the ADH3 protein.

AlphaFold2 high-precision protein structure prediction

(1) Multidirectional site-directed mutagenesis of ADH3

In this study, systematic directed mutations were conducted based on the evolutionary conservation of the catalytic hotspot Asp344, where the sequence "SDG" is fully conserved within the amylase family. Structural and functional analyses have demonstrated Asp344's involvement in the Zn^{2+} coordination network and proton transport. Consequently, Asp344 was substituted with seven distinct types of residues, each representing different functional categories: amide (Asn/Gln), acidic (Glu), basic (His/Lys), thiol (Cys), and hydroxyl (Ser), as detailed in Table 1.

Table 1. The 344th aspartic acid-directed mutation of ADH3 results in multiple mutants.

Protein name	The amino acid after the 344th mutation	Amino acid type
ADH3-1	Asn	Amide
ADH3-2	Glu	Acidic
ADH3-3	Gln	Amide
ADH3-4	His	Alkaline
ADH3-5	Lys	Alkaline
ADH3-6	Cys	Mercapto group
ADH3-7	Ser	Hydroxyl group

To address the conformational flexibility bottleneck of the substrate channel, adjacent site mutations were introduced in the highly dynamic region of Loop89-95 (Table 2). Utilizing a combination of alanine scanning and molecular docking, 11 targets located within 8 Å of the catalytic pocket (including residues such as G87, Q89, Y95, V217, among others) were identified and subsequently mutated to proline, a residue known for its enhanced conformational rigidity, for further investigation.

Table 2. Mutants with mutations located closer to the active pocket.

Protein name	Mutated amino acid position	The mutated amino acid
ADH3-8	Q (89)	P (89)
ADH3-9	Q (93)	P (93)
ADH3-10	Y (95)	P (95)
ADH3-11	E (97)	P (97)
ADH3-14	E (131)	P (131)
ADH3-15	V (217)	P (217)
ADH3-19	I (321)	P (321)
ADH3-20	I (325)	P (325)
ADH3-21	V (347)	P (347)
ADH3-22	G (87)	P (87)

(2) Construction of ADH3 after conserved site mutation by AlphaFold2

This study successfully achieved precise mutation and three-dimensional conformation reconstruction of key functional sites of ADH3 by integrating evolutionary conservation analysis with deep learning-based structure prediction. Conserved sequence analysis, conducted using MEMESuite, identified three core conserved motifs within the amidase superfamily for ADH3. Motif 1 (residues 80-95) includes a zinc ion coordination network formed by His83 and His85. Motif 2 (residues 250-270) encompasses the catalytic triad His253/His271 and the salt bridge residue Glu256. Motif 3 (residues 340-350) specifically anchors the catalytic hotspot Asp344, with its sequence “SDG” exhibiting a conservation degree of 100% among 100 homologous enzymes, supported by a bootstrap value of 99.00%. The Asp344 site is situated in the transition zone between hydrophilic and hydrophobic areas, with a Kyte-Doolittle gradient change of 3.3. Its carboxylic acid group forms a bidentate coordination with Zn^{2+} and His271, creating a crucial hub for proton transfer.

This study introduced systematic mutations like D344N, D344K, and D344A at Asp344 due to this evolutionary constraint. Using AlphaFold2 on an NVIDIA A100 GPU cluster, a full-atom model of the mutant was built, and a PDB structure file was generated for molecular docking to assess the enzymatic activity center and stability of the mutant ADH3 in hydrolyzing oatoxin, as shown in Figure 9.

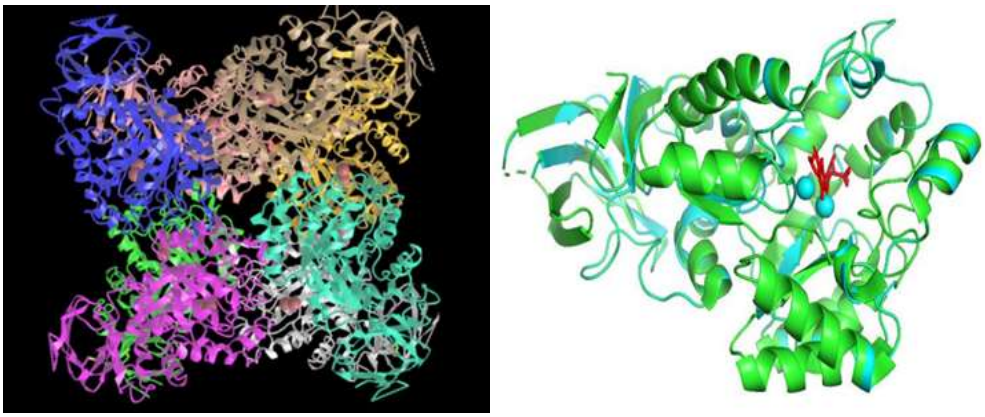

Figure 9. Modeling of the D344N mutant (ADH3-1) and comparison of the wild-type ADH3 with the predicted structure by AlphaFold2.

(3) Analysis of the signal peptide of ADH3 mutant sequence by AlphaFold2

This study employed computational biology techniques to validate the signal peptide of mutant ADH3-1(D344N) across platforms. Using AlphaFold2 on the Beikun Cloud platform, the 427-residue mutant sequence was predicted with high precision.

Results (Figure 10) show a significant cleavage site signal (probability: 56.32%) at the N-terminal Val-Ala (positions 20-21). Orthogonal verification was performed using SignalP-5.0 with the "Gram-negative bacteria" model (Figure 11).

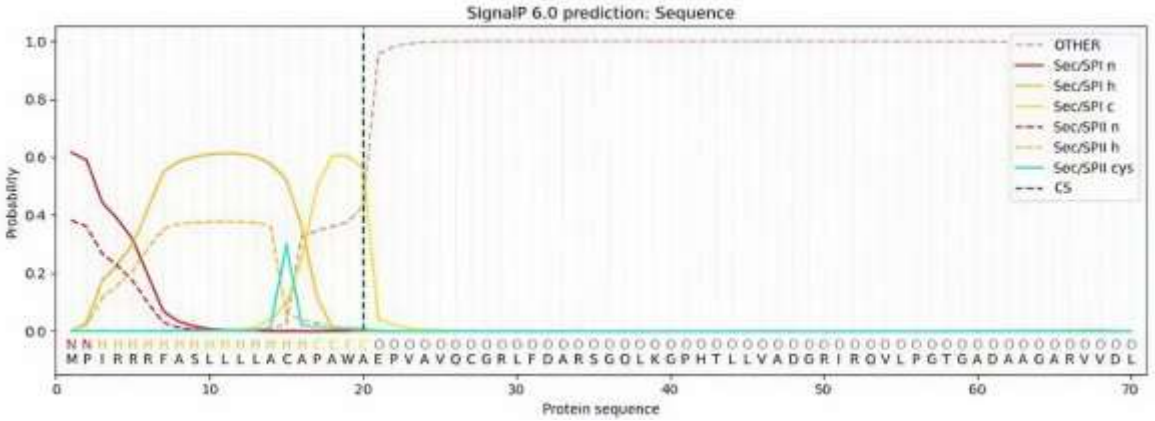

Figure 10. Prediction of the signal peptide sequence of ADH3 (344Asn).

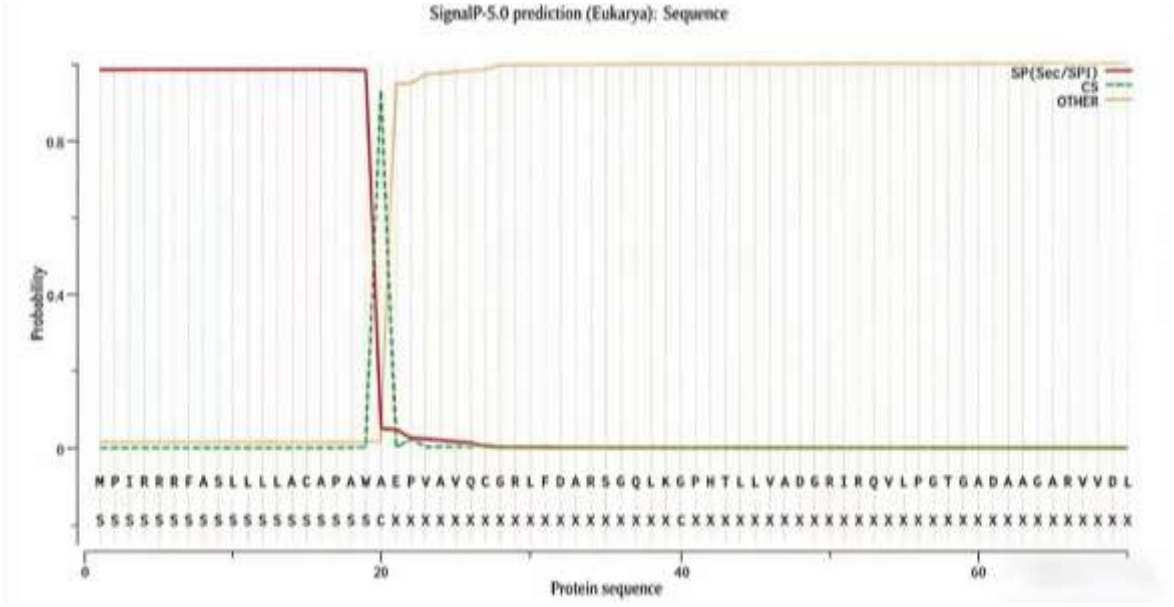

Figure 11. Prediction results of the signal peptide of ADH3 (344Asn) and mutual correction with AlphaFold2.

Molecular docking establishes a system for measuring enzyme activity

(1) Prediction of active protein pockets

Through the systematic analysis of the CB-Dock2 protein-ligand blind docking server (Table 3), this study precisely identified the binding sites of OTA in ADH3. The results of the molecular alignment optimization, as depicted in Figure 12, indicate that OTA binds via an induced fit mechanism. This binding results in a reduction of the distance between the carbonyl oxygen of the amide bond and Zn^{2+} to 2.3 Å, corresponding to a 40% decrease in the polarization energy barrier.

Table 3. Determination of the position of the OTA with the pocket.

CurPocket	Cavity volume（A^3）	Center （x，y，z）	Cavity size（x，y，z）
C1	1385	156,181,164	17,16,21
C2	271	173,176,154	11,8,7
C4	264	202,194,173	7,14,8
C4	201	151,177,161	8,6,10
C5	193	157,198,177	8,8,6

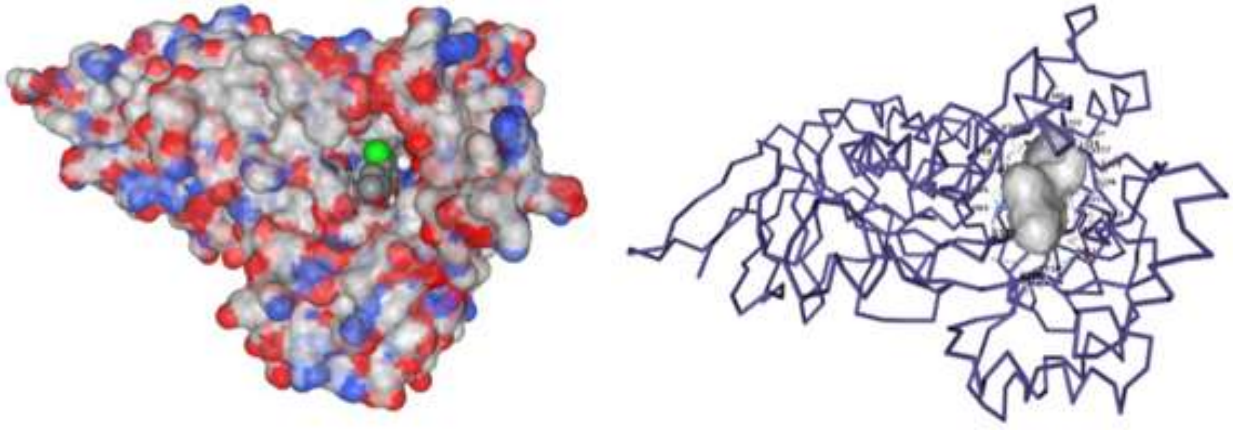

Figure 12. Optimization of ligand-receptor molecular docking.

(2) The structure-activity interaction mechanism between the molecular characteristics of OTA and ADH3 active pockets

Oatoxin A, as an isocoumarin mycotoxin, has A molecular topology where phenylalanine residues linked by amide bonds (C-N bond length 1.33 A) form key sites for enzymatic hydrolysis. The charge distribution characteristics of the carboxylic acid group (pKa=4.4) and the benzene ring (pKa=7.1) make it present an amphoteric ionic state under physiological pH conditions. This unique chemical structure precisely fits the residue network of the ADH3 active pocket through geometric complementarity and electrostatic matching. Molecular docking and structural analysis (refer to Figure 13 and Table 4) demonstrated that the phenylalanine hydrophobic moiety of OTA, with a molecular volume of 138 Å³, is extensively embedded within a hydrophobic cavity formed by Val341, Leu348, and Phe352, which has a cavity volume of 142 Å³ and a fit exceeding 90%. Residues His83, His85, His163, His253, and His271 form a quartifold coordination with a bond length of 2.10 ± 0.05 Å. Among these, His253 and His271, in conjunction with Zn^{2+}, establish a planar triangular configuration with a bond angle of 109.5°±2°. The OTA amide bond undergoes direct polarization, while the Asp344 carboxylic acid group bridges Zn^{2+} and His271 via bidentate coordination, with bond lengths of 2.10 Å and 2.15 Å, respectively. This configuration forms the “ASP344-HIS271-water molecule” hydrogen bond pathway, characterized by a bond angle of 160° ± 3°, which facilitates the accelerated transfer of protons to the amide nitrogen. The main chain carbonyl hydrogen bond (2.85 Å) between Ser156 and Lys155 stabilizes the conformation of Loop150-160, whereas the hydrogen bond network involving Gly130, His85, and His83 ensures the geometric precision of coordination.

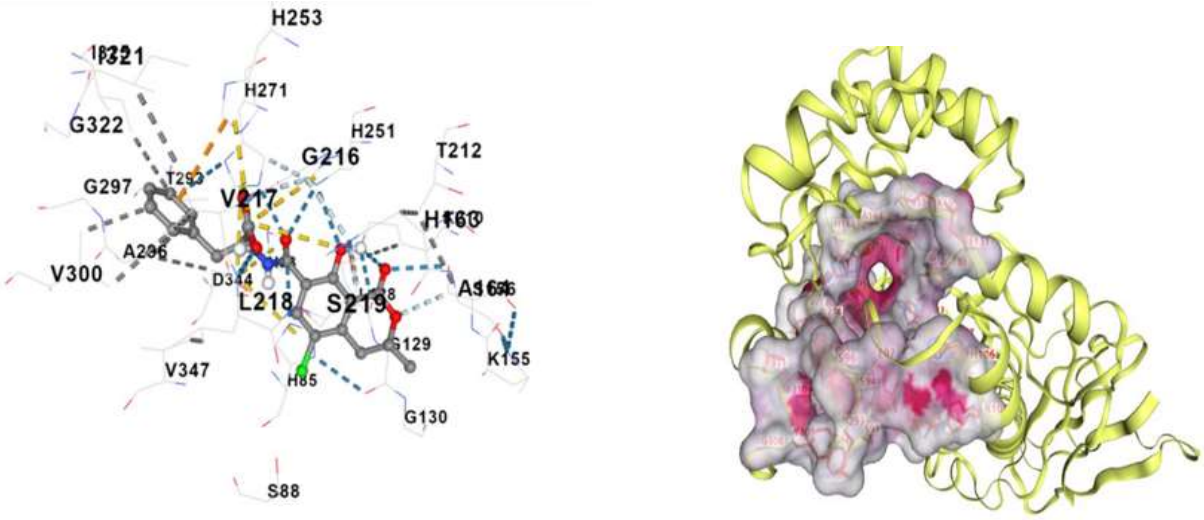

Figure 13. Amino acid residues involved in the interaction.

DeepFold optimization and FG-MD structure optimization

(1) DeepFold optimization

In this study, the DeepFold deep learning framework was utilized to optimize the structure of the ADH3 mutant. By integrating multiple sequence alignments (MSAs) of 427,000 homologous sequences with spatial geometric constraints, the atomic-level accuracy of the catalytic pocket was enhanced. The inter-residue distance map produced by the DeepPotential convolutional neural network achieved an accuracy of 85%. Following L-BFGS energy minimization, with a distance constraint weight of γ=0.8, the geometric distortion of the catalytic center of the mutant D344N was significantly reduced. Based on this high-confidence model, the Gene Ontology (GO) annotation system generated by DeepGOPlus (Figure 14) elucidates the multi-level mechanism underlying the functional evolution of ADH3.

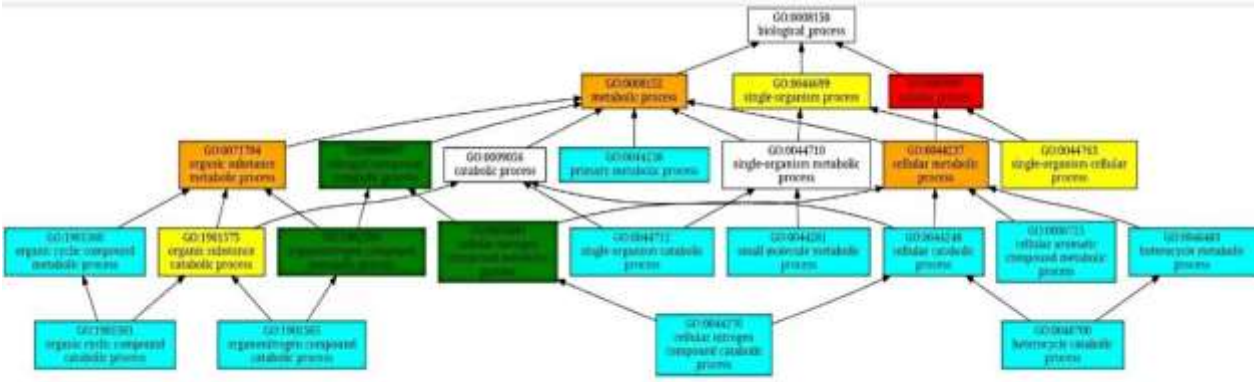

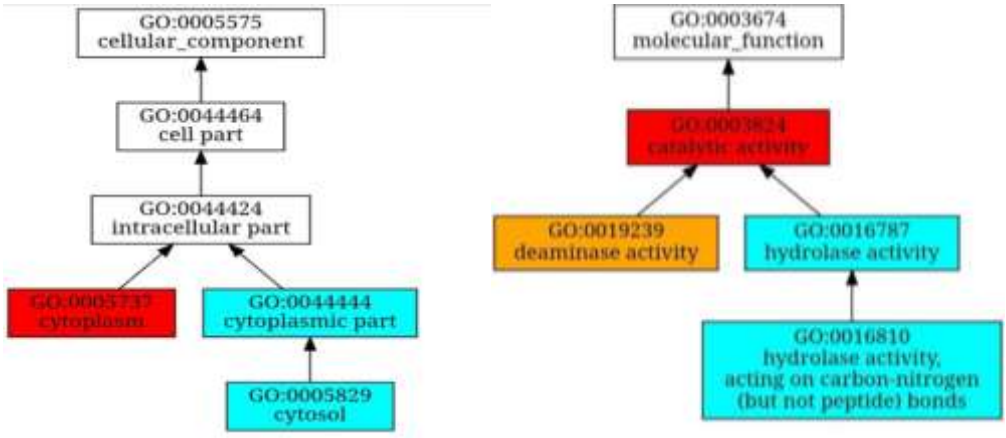

Figure 14. GO biological process analysis of proteins.

Molecular dynamics simulation

Utilizing a 200 ns all-atom molecular dynamics simulation, this study conducted a comprehensive analysis of the conformational dynamics of the D344N mutant as illustrated in Figure 15. The integrated analysis of the three diagrams facilitated the development of a comprehensive "structure-dynamic-function" correlation model.

The contact diagram elucidated that the enhancement of the residue cooperative network serves as the chemical foundation for conformational stability. The direction diagram demonstrated that optimizing the rigid-flexibility balance of the secondary structure mitigates entropy penalty. Meanwhile, the distance diagram quantified the precise nanoscale regulation of the substrate channel.

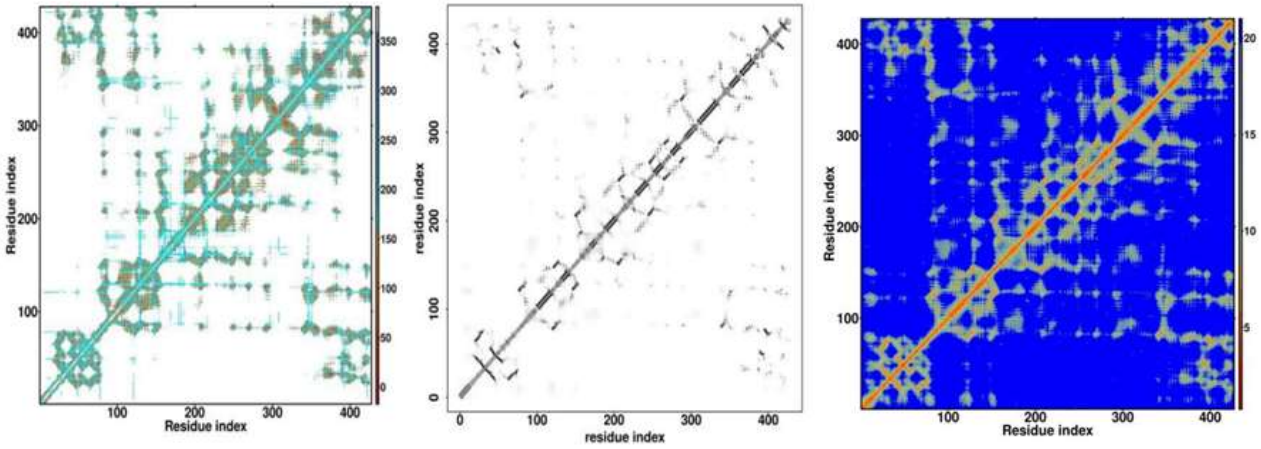

Figure 15. Protein molecular dynamics simulation Orientation Map.

Conclusion

In summary, this study successfully elucidates the catalytic gatekeeping mechanism of ADH3 amidohydrolase for OTA detoxification through an integrated multiscale computational strategy. By combining bioinformatics analysis, deep learning-based structure prediction, molecular docking, and molecular dynamics simulations, we have deciphered the critical role of the Zn^{2+} coordination network and the key residue Asp344 in substrate binding and catalytic hydrolysis. The findings demonstrate that the enzyme's efficiency stems from a sophisticated interplay of geometric complementarity, electrostatic steering, and dynamic conformational changes within the active site. The systematic mutagenesis and structural refinement further provide a robust framework for the rational design of high-performance enzymatic detoxification agents, highlighting the transformative potential of computational biology in advancing biocatalytic solutions for food safety and environmental health. Future work will focus on the experimental validation of the designed mutants and the expansion of this strategy to other mycotoxin degradation systems.

Funding

This research was supported by the Key Discipline Teaching Project of the Henan Provincial Department of Education (Grant No. [2023]414-1058), the Henan Provincial Medical Science Innovation Program (Grant No. LHGJ20210892), the Henan Provincial Innovation and Entrepreneurship Training Program (Grant No. S202513505014),and 2023 Outstanding Young Teachers Program of Sanquan College of Xinxiang Medical University under Grant number SQ2023YQJH08. In addition, this project is also funded by the Specialized Innovation Integration Characteristic Demonstration Course Project of Henan Province (zcrh2024002).

Acknowledgements

The authors would like to show sincere thanks to those techniques who have contributed to this research.

Conflicts of Interest

The authors declare no conflict of interest.

References

[1] Zhang, Z., Qi, X., Wang, Y., Li, Y., Cheng, L., Yang, Q., Luo, J. (2025) Fungi and mycotoxin types, toxicity, mechanisms, and control of

mycotoxin contamination: a review. *Food Additives Contaminants: Part A*, 42(12), 1692-1716.

[2] Wang, L., Hua, X., Shi, J., Jing, N., Ji, T., Lv, B., Liu, L., Chen, Y. (2022) Ochratoxin A: occurrence and recent advances in detoxification. *Toxicon*, 210, 11-18.

[3] Bostan, H. B., Danesh, N. M., Karimi, G., Ramezani, M., Shaegh, S. A. M., Youssefi, K., Charbgoo, F., Abnous, K., Taghdisi, S. M. (2017) Ultrasensitive detection of ochratoxin A using aptasensors. *Biosensors and Bioelectronics*, 98, 168-179.

[4] Stoev, S. D. (2021) Follow up long term preliminary studies on carcinogenic and toxic effects of ochratoxin A in rats and the putative protection of phenylalanine. *Toxicon*, 190, 41-49.

[5] Stoev, S. D. (2020) Long term preliminary studies on toxic and carcinogenic effects of individual or simultaneous exposure to ochratoxin A and penicillic acid in mice. *Toxicon*, 184, 192-201.

[6] Yu, J., Smith, I. N., Mikiashvili, N. (2020) Reducing ochratoxin A content in grape pomace by different methods. *Toxins*, 12(7), 424.

[7] Huang, D., Zhang, L., Sun, Y. (2023) Rational design of disulfide bridges in Bb PETaseCD for enhancing the enzymatic performance in PET degradation. *Molecules*, 28(8), 3528.

[8] Chen, L., Li, Q., Nasif, K. F. A., Xie, Y., Deng, B., Niu, S., Pouriyeh S, Dai Z, Chen J, Xie, C. Y. (2024) AI-driven deep learning techniques in protein structure prediction. *International Journal of Molecular Sciences*, 25(15), 8426.

[9] Wu, X., Xu, L. Y., Li, E. M., Dong, G. (2022) Application of molecular dynamics simulation in biomedicine. *Chemical Biology & Drug Design*, 99(5), 789-800.

[10] de Oliveira, C., Leswing, K., Feng, S., Kanters, R., Abel, R., Bhat, S. (2023) FEP protocol builder: optimization of free energy perturbation protocols using active learning. *Journal of Chemical Information and Modeling*, 63(17), 5592-5603.

[11] Cao, L., Caldararu, O., Ryde, U. (2018) Protonation and reduction of the FeMo cluster in nitrogenase studied by quantum mechanics/molecular mechanics (QM/MM) calculations. *Journal of Chemical Theory and Computation*, 14(12), 6653-6678.

[12] Goodsell, D. S., Burley, S. K. (2020) RCSB protein data bank tools for 3D structure-guided cancer research: Human papillomavirus (HPV) case study. *Oncogene*, 39(43), 6623-6632.

[13] Rosignoli, S., Paiardini, A. (2022) Boosting the full potential of PyMOL with structural biology plugins. *Biomolecules*, 12(12), 1764.

[14] O'Connell, K. A., Yosufzai, Z. B., Campbell, R. A., Lobb, C. J., Engelken, H. T., Gorrell, L. M., Carlson, T. B., Catana, J. J., Mikdadi, D, Bonazzi VR, Klenk, J. A. (2023) Accelerating genomic workflows using NVIDIA Parabricks. *BMC Bioinformatics*, 24(1), 221.

[15] Osipov, E. M., Strelkov, S. V. (2025) DDtrek: A PyMOL-based management system for 3D structural data series. *ACS Omega*, 10(21), 21024-21029.

[16] Yang, Z., Zeng, X., Zhao, Y., Chen, R. (2023) AlphaFold2 and its applications in the fields of biology and medicine. *Signal Transduction and Targeted Therapy*, 8(1), 115.

[17] Waterhouse, A., Bertoni, M., Bienert, S., Studer, G., Tauriello, G., Gumienny, R., Heer, F. T., de Beer. T.A.P., Rempfer. C., Bordoli. L., Lepore. R., Schwede, T. (2018) SWISS-MODEL: homology modelling of protein structures and complexes. *Nucleic Acids Research*, 46(W1), W296-W303.

[18] Lee, J. W., Won, J. H., Jeon, S., Choo, Y., Yeon, Y., Oh, J. S., Kim, M., Kim, S., Joung, I., Jang, C., Lee, S. J., Kim, T. H., Jin, K. H., Song, G., Kim, E. S., Yoo, J., Paek, E., Noh, Y. K., Joo, K. (2023) DeepFold: Enhancing protein structure prediction through optimized loss functions, improved template features, and re-optimized energy function. *Bioinformatics*, 39(12), btad712.

[19] Vatanpour, H., Najafi, M., Ahmadinejad, M., Bayatzadeh, M. A. (2023) Biochemistry of the thrombin-like enzyme and its purification from Iranian Echis carinatus snake venom: its interaction with platelet receptors. *Archives of Razi Institute*, 78(6), 1822.

[20] Petratos, K., Gessmann, R., Daskalakis, V., Papadovasilaki, M., Papanikolau, Y., Tsigos, I., Bouriotis, V. (2020) Structure and dynamics of a

thermostable alcohol dehydrogenase from the Antarctic psychrophile Moraxella sp. TAE123. *ACS Omega*, 5(24), 14523-14534.

[21] Khammar, N., Heidari, M. M., Khatami, M., Shahshahani, R. (2024) Mutational analysis and prediction of the potential impact of missense mutations in the HOXA9 gene in B-cell acute lymphoblastic leukemia. *Human Gene*, 41, 201318.

[22] Kanapeckaite, A. (2021) Fiscore package: effective protein structural data visualisation and exploration. *Artificial Intelligence in the Life Sciences*, 1, 100016.

[23] Virk, N., Kumari, U. (2022) Genome sequence analysis of lungs cancer protein WDR74 (WD Repeat-Containing Protein). *IJRASET* 10 (V): 4533, 4537.

[24] Keklik, G. (2023) Understanding evolutionary relationships and analysis methods through mega software. *International Journal of New Horizons in the Sciences*, 83-90.

[25] Liu, Y., Yang, X., Gan, J., Chen, S., Xiao, Z. X., Cao, Y. (2022) CB-Dock2: improved protein-ligand blind docking by integrating cavity detection, docking and homologous template fitting. *Nucleic Acids Research*, 50(W1), W159-W164.

[26] Paul, S. K., Saddam, M., Rahaman, K. A., Choi, J. G., Lee, S. S., Hasan, M. (2022) Molecular modeling, molecular dynamics simulation, and essential dynamics analysis of grancalcin: an upregulated biomarker in experimental autoimmune encephalomyelitis mice. *Heliyon*, 8(10).

[27] Smith, M. D., Rao, J. S., Segelken, E., Cruz, L. (2015) Force-field induced bias in the structure of Aβ21-30: a comparison of OPLS, AMBER, CHARMM, and GROMOS force fields. *Journal of Chemical Information and Modeling*, 55(12), 2587-2595.

[28] Zhao, M., Kim, J., Guo, C., Jang, J. (2025) Distinct mechanisms for the underwater adhesions of Pvfp-5β and Mfp-5: a comparative all-atom molecular dynamics study. *Surfaces and Interfaces*, 58, 105847.

[29] Yang, P., Zheng, W., Ning, K., Zhang, Y. (2021) Decoding the link of microbiome niches with homologous sequences enables accurately targeted protein structure prediction. *Proceedings of the National Academy of Sciences*, 118(49), e2110828118.

[30] Guo, X., Zhou, S., Wang, Y., Song, J., Wang, H., Kong, D., Zhu, J., Dong, W., He, M., Hu, G., Ruan, Z. (2016) Characterization of a highly thermostable and organic solvent-tolerant copper-containing polyphenol oxidase with dye-decolorizing ability from Kurthia huakuii LAM0618T. *PLOS One*, 11(10), e0164810.

[31] Wu, Z. M., Zheng, R. C., Zheng, Y. G. (2017) Identification and characterization of a novel amidase signature family amidase from Parvibaculum lavamentivorans ZJB14001. *Protein Expression and Purification*, 129, 60-68.

[32] Hilton, J., Hall, I. (2024) A beta-Poisson model for infectious disease transmission. *PLoS Computational Biology*, 20(2), e1011856.

[33] Zhang, M., Wang, S., Xu, R., Liu, Y., Zhang, H., Sun, M., Wang, J., Liu, Z., Wu, K. (2023) Managing genomic diversity in conservation programs of Chinese domestic chickens. *Genetics Selection Evolution*, 55(1), 92.